Contents lists available at ScienceDirect

Applied Catalysis B: Environmental

A new low-temperature solution route to Aurivillius-type layered oxyfluoride perovskites Bi_2MO_5F (M = Nb, Ta) as photocatalysts

Shuijin Lei [a,*], Di Cheng [a], Xijie Gao [a], Linfeng Fei [b], Wei Lu [b], Jianliang Zhou [c], Yanhe Xiao [a], Baochang Cheng [a], Yu Wang [a], Haitao Huang [b,*]

[a] School of Materials Science and Engineering, Nanchang University, Nanchang, Jiangxi, 330031, China
[b] Department of Applied Physics, The Hong Kong Polytechnic University, Hong Kong Special Administrative Region, China
[c] Department of Cardiothoracic Surgery, The Second Affiliated Hospital of Nanchang University, Nanchang, Jiangxi, 330006, China

ARTICLE INFO

ABSTRACT

Aurivillius oxyfluoride perovskites exhibit great potential in photocatalysis, which are generally prepared by high-temperature solid-state reactions and some impurity phases are always unavoidable. Herein, a new low-temperature solution method has been successfully developed for the synthesis of Bi_2NbO_5F and Bi_2TaO_5F pure phases. The electron microscopy results reveal that the products were composed of the hierarchical hollow spheres with porous surface. The formation and growth mechanisms of the products were proposed based on the time-dependent evolution. The experimental band gaps of Bi_2NbO_5F (2.86 eV) and Bi_2TaO_5F (2.95 eV) were also first obtained. The photodegradation tests demonstrated that the products could be effectively served as catalysts for degradation of Rhodamine B and methyl orange under UV-light irradiation via the photocatalytic reaction, and also could be used in visible-light degradation of Rhodamine B via the photosensitization process. This low-temperature solution preparation of Aurivillius oxyfluorides opens a new facile route to tackle the versatile chemistry of various oxyfluoride perovskites.

1. Introduction

It is well known that the ABO_3 perovskites have rich variety of structural, electronic and magnetic properties. In a broader context, this type of structure also includes the layered perovskites, such as Aurivillius (AV), Dion-Jacobson (DJ), and Ruddlesden-Popper (RP) –type phases [1]. Aurivillius compounds, a family of layered bismuth oxide materials, can be represented by the general formula $Bi_2A_{n-1}B_nO_{3n+3}$, which are constructed by n perovskite $(A_{n-1}B_nO_{3n+1})^{2-}$ layers regularly interleaved with a fluorite-like $(Bi_2O_2)^{2+}$ layer [2]. The layered perovskites, particularly the RP phases $(A_{n-1}B_nO_{3n+1})$, have been extensively studied due to the persistent search for high-T_c superconductive materials. Considering the structural similarity between AV and RP phases, it was suggested that some AV compounds are also superconductors [3,4]. Generally, owing to the good adoptability of cation sites, the chemical compositions and physical properties of these layered perovskites can be well controlled. However, most researches

have been focused on the cation substitution, while little attention has been paid to manipulate the anion lattice to control the structural and physical properties. Actually, based on the strong effects of the anion on the crystal field and electronic state of the metal center, the anion substitution has potential for enhancing the original physical properties or inducing new exotic phenomena, thanks to the different bonding nature, valence state and ionic radius from that of oxygen [1]. Taking Bi_2NbO_6 as the representative, Medvedeva et al. demonstrated that ideal Bi_2NbO_6 is unstable and tends to contain massive oxygen vacancies. As a result, partial replacement of O by F would be energetically favorable, such as in the case of fluorinated phase Bi_2NbO_5F [5,6].

Three kinds of F-containing AV-type compounds such as Bi_2NbO_5F, Bi_2TaO_5F and $Bi_2TiO_4F_2$ were firstly synthesized by Aurivillius, and a body-centered tetragonal structure ($I4/mmm$) was determined [7]. Recently, although Needs et al. still adopted the same space group, they thought the structures of Bi_2NbO_5F and $Bi_2TiO_4F_2$ are not as ideal as reported by Aurivillius according to the anion distributions or atomic positions [8]. Later, McCabe et al. proposed a lower symmetry orthorhombic space group $Pbca$ for the Bi_2NbO_5F phase [9]. Based on bond valence calculations, Needs et al. [8] considered that F atoms tend to locate in the equatorial sites of $Nb(O,F)_6$ or $Ti(O,F)_6$ octahedra, but McCabe et al. [9]

* Corresponding authors.
E-mail addresses: shjlei@ncu.edu.cn (S. Lei), aphhuang@polyu.edu.hk (H. Huang).

suggested that F atoms prefer the apical sites for Bi_2NbO_5F. It has been reported that these three phases are ferroelectrics with Curie temperatures of 303, 283 and 284 K, respectively [10,11], but the relationship between the crystal structure and the ferroelectricity is still controversial. Unfortunately, the physichemical properties of Bi_2NbO_5F and Bi_2TaO_5F are rarely reported. Recently, the electronic band structure of Bi_2NbO_5F has been investigated by theoretical computation [12,13], proving that Bi_2NbO_5F is a ferroelectric semiconductor with a narrow indirect band gap. However, there still lack the corresponding experimental data to support these theoretical results. Traditionally, these AV-type layered oxyfluoride perovskites, Bi_2MO_5F (M = Nb, Ta) and $Bi_2TiO_4F_2$, were prepared via high-temperature solid-state reactions [7–11]. However, some impurity phases, such as BiF_3, Bi_2O_3 and BiOF, are always unavoidable. Kodama et al. reported that the pure Bi_2NbO_5F and $Bi_2TiO_4F_2$ phases can be prepared by hydrothermal method under high temperature ($\geq 400\,°C$) and high pressure ($\geq 500\,kg\,cm^{-2}$) [14]. Using this method, Needs et al. prepared almost pure phases of Bi_2NbO_5F and $Bi_2TiO_4F_2$ with a small quantity of BiOF and TiO_2. The oxyfluoride perovskite could be the major phase only when the mass of reactants was exactly equal to that of 1 M NH_4F solution [8]. Besides high temperature, high pressure and long reaction time, the reaction vessel used for this hydrothermal experiment was also severe, where the starting materials and solvent were placed in gold and platinum capsules, respectively. Although the low-temperature hydrothermal/solvothermal route has been successfully employed in the synthesis of $Bi_2TiO_4F_2$ [15,16], it should be noted that the low-temperature solution synthesis of Bi_2NbO_5F and Bi_2TaO_5F has never been reported.

Considering that semiconductor photocatalysis is one of the advanced physicochemical processes applied in environmental remediation (e.g. pollutant degradation) and clean energy production (e.g. hydrogen production), many kinds of semiconductors have been exploited as photocatalytic materials, such as oxides, sulfides, oxysulfides, nitrides, oxynitrides and so on [17–22]. Among them, bismuth compounds have attracted great interest in the area of catalytic photodegradation over the past decades. In Bi-based compounds, Bi^{3+} ions have the stereochemically active $6s^2$ lone electron pairs. The intrinsic polarization of these electrons has been proven to be effective for the separation and easy transfer of photogeneraed electrons and holes [23]. In this case, a great deal of effort has been devoted to the exploration of Bi-based photocatalysts [24]. On the other hand, a host of perovskite materials also have been observed to be promising in photocatalysis and photovoltaics since the layered structure is also beneficial to the separation of photogenerated electrons and holes [25]. Therefore, Aurivillius compounds have been deservedly expected for application in photocatalysis [26–31]. Furthermore, in AV-type oxyfluorides, the existence of F atom can effectively reduce the recombination of photogenerated electrons and holes due to its strong electronegativity, thus improving photocatalytic performance [15]. Overall, the AV-type layered oxyfluoride perovskites possess multiple advantages in photocatalysis. In the three AV-type layered oxyfluoride perovskites, only $Bi_2TiO_4F_2$ has been investigated as photocatalyst [15,16]. However, previous researches on Bi_2NbO_5F and Bi_2TaO_5F were mainly focused on their crystal structure and ferroelectric behaviour. To the best of our knowledge, their photocatalytic properties have never been reported because of the difficulty in preparation.

In this work, Bi_2NbO_5F and Bi_2TaO_5F pure phases were synthesized by a solvothermal method at only $150\,°C$, using acid heptafluorniobic aqueous solution and $Bi(NO_3)_3$ ethylene glycol solution as the starting materials. The formation and growth mechanism were investigated based on the time-dependent phase and morphology evolution experiments. More importantly, the experimental bandgaps of the products were also first obtained and the photocatalytic properties were studied under both UV- and visible-light irradiation.

2. Experimental

2.1. Chemicals and materials

All the chemicals were used as received without any further purification. Niobium pentoxide (Nb_2O_5, 99.99%), Tantalum pentoxide (Ta_2O_5, 99.99%), ethylene glycol ($OH(CH_2)_2OH$, analytical grade), Rhodamine B ($C_{28}H_{31}ClN_2O_3$, analytical grade), and methyl orange ($C_{14}H_{14}N_3SO_3Na$, analytical grade) were purchased from Sinopharm Chemical Reagent Co., Ltd. (Shanghai, China). Pentahydrated bismuth nitrate ($Bi(NO_3)_3\cdot 5H_2O$, analytical grade) and hydrofluoric acid (HF, 40%) were obtained from Xilong Chemical Co., Ltd. (Shantou, China).

2.2. Synthesis of Bi_2MO_5F (M = Nb, Ta)

All samples were prepared by a facile solvothermal process. In a typical synthesis, 0.5 mmol of Nb_2O_5 (or Ta_2O_5) was dissolved in 5 mL of HF at $90\,°C$ with oil bath. To volatilize the excess HF, the clear solution was maintained at this temperature for evaporation. When only $1 \sim 2$ mL solution remained, 20 mL distilled water was then added to dilute it, and the solution continued to evaporate. The dilution and evaporation procedures were repeated for more than 20 times to completely remove HF as far as possible. Finally, the solution was diluted to 10 mL. On the other hand, 2 mmol of $Bi(NO_3)_3$ was dissolved into 30 mL of ethylene glycol (EG). Subsequently, the Nb(Ta)-based solution was added dropwise into $Bi(NO_3)_3$ solution under continuous magnetic stirring. The resulting mixture was further stirred and incubated for about 30 min and then transferred into a stainless steel Teflon-lined autoclave of 50 mL capacity. The autoclave was sealed and maintained at $150\,°C$ for 12 h, and then cooled to room temperature naturally. The precipitates were filtered off and washed with absolute ethanol and distilled water several times to remove the organic residues and soluble impurities. After dried at $60\,°C$ for 5 h in air, a pale yellow powder was obtained.

2.3. Sample characterization

X-ray powder diffraction (XRD) patterns were recorded on a Rigaku SmartLab Intelligent X-ray diffraction system with filtered Cu Kα radiation ($\lambda = 1.5406$ Å, operating at 45 kV and 200 mA) and a PANalytical Empyrean diffractometer with Cu Kα radiation ($\lambda = 1.5406$ Å, operating at 40 kV and 40 mA). The core level X-ray photoelectron spectroscopy (XPS) and valence band X-ray photoelectron spectroscopy (VB-XPS) analyses were carried out using an ESCALAB 250Xi X-ray photoelectron spectrometer with Al Kα monochromatic radiation at a constant pass energy of 1486.6 eV (ThermoFisher Scientific, USA). Scanning electron microscopy (SEM) measurements were preformed on a Quanta 200F environmental scanning electron microscope (FEI, Netherlands). Field-emission scanning electronic microscopy (FE-SEM) observations were carried out on a JEM-6335F field-emission system (JEOL, Japan). Transmission electron microscopy (TEM) images, high resolution transmission electron microscopy (HRTEM) images, selected area electron diffraction (SAED) patterns, energy dispersive X-ray spectroscopy (EDS) spot scan spectra and elemental mapping were taken from a JEM-2100F (field emission) scanning transmission electron microscope (JEOL, Japan) with an acceleration voltage of 200 kV. During TEM tests, after ultrasonic agitation, one or more drops of the ethanol solution containing the as-synthesized sample were deposited onto the amorphous carbon

film supported on a copper grid and allowed to dry at room temperature in air. The ultraviolet-visible (UV–vis) diffuse reflectance spectra were obtained on a UV-2550 UV–vis spectrophotometer (Shimadzu, Japan) equipped with an integrating sphere accessory using barium sulfate as a reference material. The nitrogen adsorption-desorption isotherms were measured on a Micromeritics ASAP-2000 nitrogen adsorption apparatus. The surface area was calculated by the Brunauer-Emmett-Teller (BET) method and the pore size distribution was calculated using the Barrett-Joyner-Halenda (BJH) model.

2.4. Photocatalytic activity test

The photocatalytic performance of the as-synthesized samples was evaluated through photodegradation of Rhodamine B (RhB) and Methyl Orange (MO) under both UV-light and visible-light irradiation at room temperature. A 300 W Xenon lamp (HSX-F/UV300, Beijing NBeT Technology Co., Ltd.) was used as the light source with a UVREF filter (200∼400 nm) to provide UV light and with an ultraviolet cutoff filter (λ ≥ 400 nm) to provide visible light irradiation. The catalytic reaction was carried out in a closed quartz cell with a capacity of 500 mL, and the system temperature was controlled with a circulating water cooling system on the reaction cell. In each test, 0.2 g of the as-prepared powder catalyst was dispersed into 100 mL of dye aqueous solution (RhB or MO) with an initial concentration of 10 mg L^{-1}. Prior to illumination, the suspension was vigorously stirred in the dark for 30 min to ensure the adsorption–desorption equilibrium between catalyst and dye. The suspension was then stirred and exposed to the light irradiation. At every 10 min interval, approximately 5 mL of the suspension was collected and centrifuged to remove the catalyst until the color of solution became colorless. The concentration of dye was analyzed using a TU-1810 UV–vis spectrophotometer (Purkinje General, China) at λ = 554 nm (for RhB) and λ = 464 nm (for MO). Total organic carbon (TOC) concentrations during photolysis were also assayed on a TOC-L CPH/CPN total organic carbon analyzer (Shimadzu, Japan). TOC values were calculated as the difference between the total carbon (TC) and inorganic carbon (IC) in the aqueous solution samples.

3. Results and discussion

3.1. Phase analysis

Fig. 1 presents the typical XRD patterns of the as-synthesized products. In Fig. 1a, it shows that all the diffraction peaks can be indexed to tetragonal structure of Bi$_2$NbO$_5$F with lattice constants of a = 3.839 Å and c = 16.638 Å, which are perfectly consistent with the reported data (JCPDS Card File No. 73−2190, a = 3.835 Å and c = 16.630 Å). No characteristic reflection peaks originated from other impurity phases such as Nb$_2$O$_5$, Bi$_2$O$_3$, BiF$_3$, BiOF or bismuth niobates can be detected, which indicates that it should be Bi$_2$NbO$_5$F pure phase. The XRD pattern in Fig. 1b is very close to that in Fig. 1a, suggesting that Bi$_2$TaO$_5$F has the same crystal structure as that of Bi$_2$NbO$_5$F. Accordingly, the cell parameters of Bi$_2$TaO$_5$F are calculated to be a = 3.841 Å and c = 16.739 Å. The simulated XRD lines using the calculated lattice parameters and the Bi$_2$NbO$_5$F crystal structure (Fig. S1) give a good match to the experimental diffraction pattern, which suggests the pure phase of Bi$_2$TaO$_5$F. In order to further prove the phase identity, the Rietveld refinements of the Bi$_2$NbO$_5$F and Bi$_2$TaO$_5$F XRD data were also conducted. The corresponding refinement results for Bi$_2$NbO$_5$F and Bi$_2$TaO$_5$F samples are displayed in Fig. S2 and S3, respectively. It can be seen that a good fitting can be achieved between the experimental and calculated patterns. The phase compositions of the Bi$_2$NbO$_5$F and
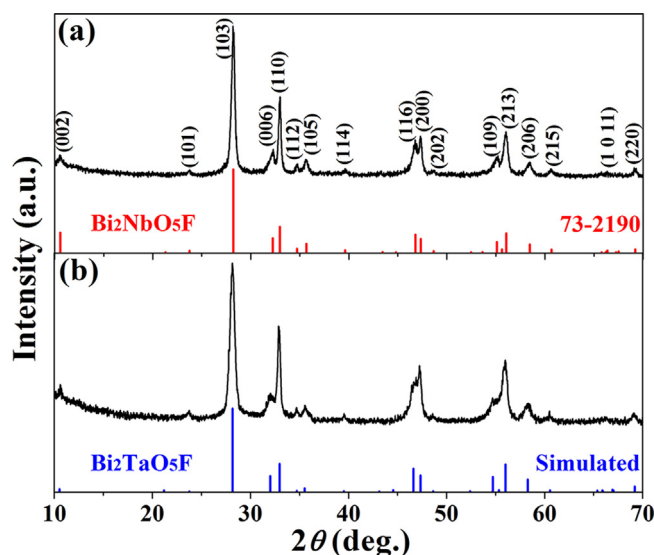
Fig. 1. XRD patterns of the as-prepared (a) Bi$_2$NbO$_5$F and (b) Bi$_2$TaO$_5$F samples.

Bi$_2$TaO$_5$F samples were further determined by the XPS analyses as shown in Fig. S4 and S5. The XPS survey spectra indicate the presence of Bi, Nb(Ta), O, and F as well as C impurity. Carbon signal may be derived from the reference. The high-resolution XPS spectra were investigated in the Bi 4f, Nb 3d, Ta 4f, O 1s and F 1s regions. All these core level spectra are in good agreement with the literature values [32]. Therefore, it should be convinced that the prepared samples are Bi$_2$NbO$_5$F and Bi$_2$TaO$_5$F pure phases.

3.2. Morphology and component analyses

Fig. 2a and b present the SEM images of Bi$_2$NbO$_5$F and Bi$_2$TaO$_5$F, respectively. Both samples consist of spheres with diameters of about 1∼2 μm, which exhibit a hierarchical hollow structure, composed of nanoflakes to form the porous surface. The enlarged SEM images of both samples are provided in Fig. S6. Consistent with SEM observations, the TEM images (Fig. 2c and d) further demonstrate the hollow hierarchical spherical structure, and the wall thickness of the spheres is approximately 200 nm. To further explore the microstructure of the two samples, HRTEM and SAED were carried out. As shown in Fig. 2e and f, the clear one-dimensional lattice fringes in HRTEM images can be observed. The interplanar spacings can be measured to be around 0.32 nm, which match well with the (103) planes of tetragonal structure of Bi$_2$NbO$_5$F and Bi$_2$TaO$_5$F. The corresponding SAED patterns are presented in the insets of Fig. 2e and f. The diffraction rings from inner to outer can be indexed as (103), (110)/(006), (200)/(116), (109) and (219) reflections, respectively, corresponding to tetragonal Bi$_2$NbO$_5$F and Bi$_2$TaO$_5$F, which are also in good agreement with XRD results. The structural composition of the as-synthesized products was investigated via the EDS analyses. As shown in Fig. S7 and S8, the elemental mapping images exhibit a uniform distribution of Bi, Nb(Ta), O, and F elements, and the EDS spectra give the atomic ratio of Bi:Nb(Ta) near 2:1. These results further confirm the formation of Bi$_2$NbO$_5$F and Bi$_2$TaO$_5$F phases.

3.3. Formation and growth mechanism analyses

In order to reveal the formation and growth process of the obtained Bi$_2$NbO$_5$F and Bi$_2$TaO$_5$F hierarchical hollow spheres, the phase evolution was characterized as a function of time. Taking Bi$_2$TaO$_5$F as an example, it can be seen that when the reaction time is only 1 h, all diffraction peaks can be easily indexed to
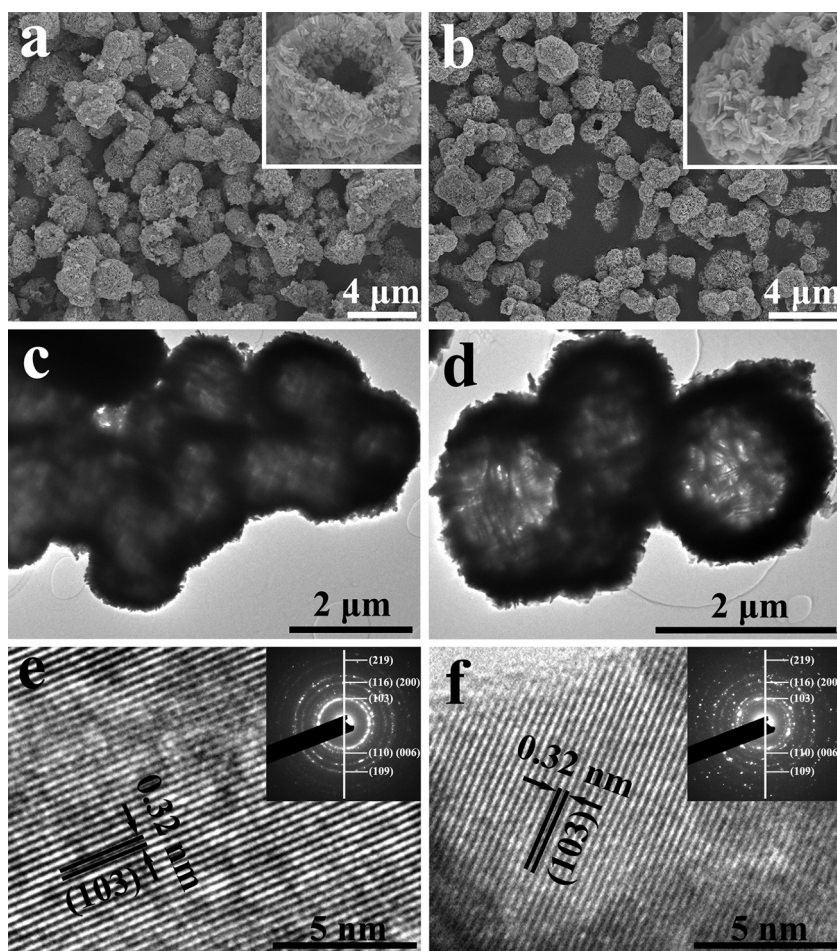
Fig. 2. (a) SEM, (c) TEM, and (e) HRTEM images of the as-prepared Bi_2NbO_5F sample; (b) SEM, (d) TEM, and (f) HRTEM images of the as-prepared Bi_2TaO_5F sample. The insets in (e) and (f) are the corresponding SAED patterns.

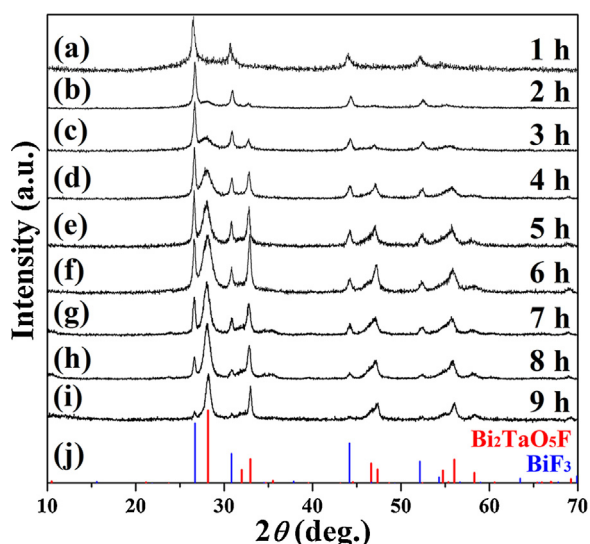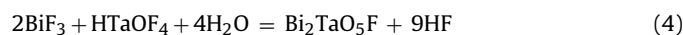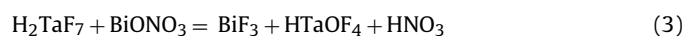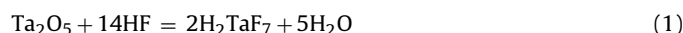**Fig. 3.** XRD patterns of the phase evolution for Bi_2TaO_5F samples prepared at different reaction time: (a-i) 1–9 h. (j) theoretical XRD patterns of Bi_2TaO_5F (red line) and BiF_3 (blue line). (For interpretation of the references to colour in this figure legend, the reader is referred to the web version of this article.)

the cubic BiF_3 phase (Fig. 3). As the reaction time is prolonged to 2 h, small diffraction peaks of the Bi_2TaO_5F phase (e.g. 28.2°, 33.0°) can be detected. With longer reaction time, the diffraction

peaks of Bi_2TaO_5F become stronger, while those of BiF_3 weaker. When it reaches 7 h, Bi_2TaO_5F becomes the major phase. Until 9 h, only a small quantity of BiF_3 phase is left. As previously mentioned, Bi_2TaO_5F pure phase can be prepared for a reaction time of 12 h. Based on the above results, the formation of Bi_2TaO_5F phase can be summarized into four major steps: (i) acid heptafluortantalic (H_2TaF_7) complex solution formed by dissolution of Ta_2O_5 into HF acid; (ii) $Bi(NO_3)_3$ hydrolyzed to form bismuth oxynitrate ($BiONO_3$); (iii) BiF_3 formed through the reaction of H_2TaF_7 and $BiONO_3$, together with the generation of $HTaOF_4$; (iv) the resultant BiF_3 and unreacted $BiONO_3$ sequentially reacted with $HTaOF_4$ to form Bi_2TaO_5F phase. The reaction equations are proposed as follows:

$$Ta_2O_5 + 14HF = 2H_2TaF_7 + 5H_2O \tag{1}$$

$$Bi(NO_3)_3 + H_2O = BiONO_3 + 2HNO_3 \tag{2}$$

$$H_2TaF_7 + BiONO_3 = BiF_3 + HTaOF_4 + HNO_3 \tag{3}$$

$$2BiF_3 + HTaOF_4 + 4H_2O = Bi_2TaO_5F + 9HF \tag{4}$$

$$2BiONO_3 + HTaOF_4 + 2H_2O = Bi_2TaO_5F + 3HF + 2HNO_3 \tag{5}$$

Therefore, to describe the whole solvothermal reaction, Eqs. (2)–(5) can be combined into one single equation:

$$H_2TaF_7 + 2Bi(NO_3)_3 + 5H_2O = Bi_2TaO_5F + 6HNO_3 + 6HF \tag{6}$$

The situations for Bi_2NbO_5F are regarded to be similar to Bi_2TaO_5F. However, It was noted in our previous research that the final product is BiF_3–Bi_2NbO_5F composite, instead of a single
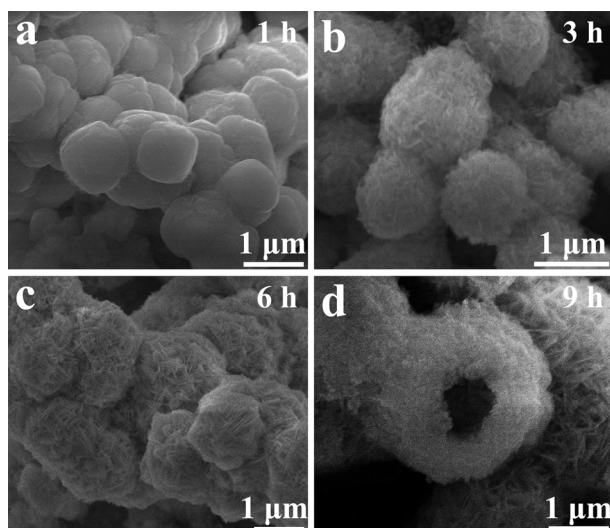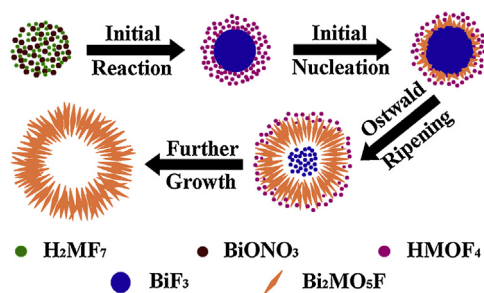
Fig. 4. SEM images of the morphology evolution of for Bi_2TaO_5F samples prepared at different reaction time: (a) 1 h, (b) 3 h, (c) 6 h, and (d) 9 h.

Scheme 1. Schematic illustration of the morphological evolution for the Bi_2MO_5F hierarchical hollow spheres at various stages.

Fig. 5. Nitrogen adsorption-desorption isotherms of the as-prepared (a) Bi_2NbO_5F and (b) Bi_2TaO_5F hierarchical hollow spheres. The insets present the corresponding pore size distribution curves deduced from the desorption branch.

phase Bi_2NbO_5F [33]. Comparing the two synthesis methods, it can be seen that the main difference is the evaporation process of HF acid when preparing H_2NbF_7 precursor solution. Therefore, the HF content in reactants is determinant for the phase of final product. Experiments showed that the pure single phase of Bi_2NbO_5F or Bi_2TaO_5F could be obtained when HF was removed as completely as possible. According to Eq. (4), with the complete evaporation of HF, the chemical equilibrium will shift towards the products, leading to the complete reaction of BiF_3 phase ultimately.

To explore a possible growth mechanism of the hierarchical hollow spheres, the morphology evolution was also studied as shown in Fig. 4. Accordingly, a possible growth mechanism is also proposed as illustrated in Scheme 1. Initially, BiF_3 spheres were formed based on the reaction of Eq. (3) (Fig. 4a). It is always possible that the conventional self-assembly process in aqueous solution phase makes for spherical crystals to diminish the surface energy. With increasing reaction time, $HTaOF_4$ solution around BiF_3 spheres consequentially reacted with BiF_3 spheres on their surface (Eq. (4)). As a result, Bi_2TaO_5F nanoplates formed on the surface of BiF_3 spheres (Fig. 4b). Additionally, the reaction of Eq. (5) could further support the formation of Bi_2TaO_5F nanoplates. As time and reactions (Eqs. (4) and (5)) went on, based on Ostwald ripening, more and larger Bi_2TaO_5F nanoplates would be developed with the gradual consumption of BiF_3 (Fig. 4c). With further growth and total dissolution of BiF_3, the hierarchical Bi_2TaO_5F hollow spheres could be obtained eventually (Fig. 4d).

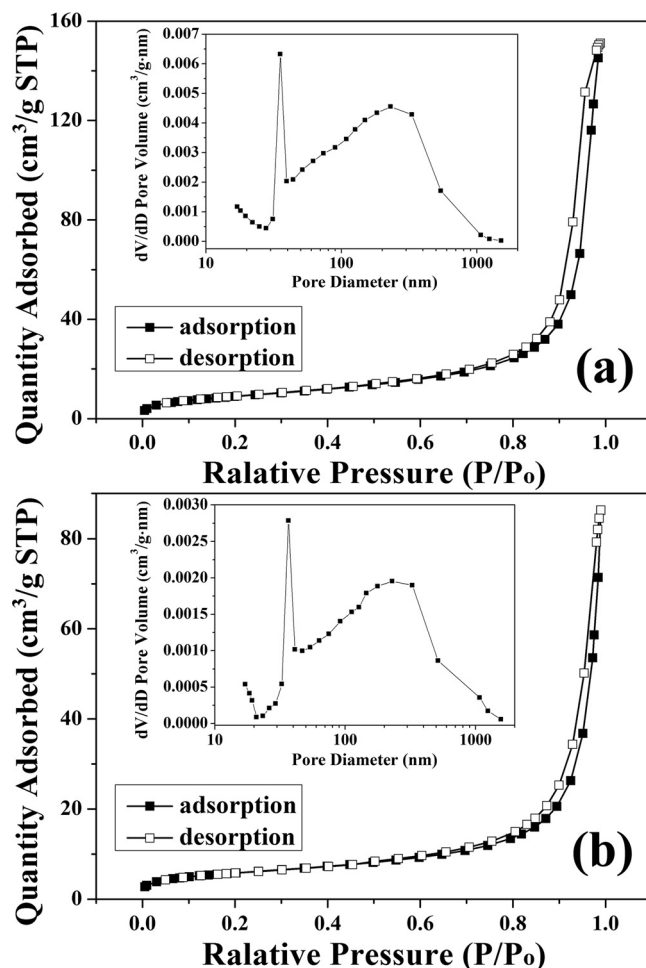### 3.4. Surface area and porosity analyses

It is generally accepted that hierarchical hollow spheres are likely to possess the advantage of high surface area. It can be seen from Fig. 5 that the adsorption-desorption isotherms of both Bi_2NbO_5F and Bi_2TaO_5F samples exhibit type-IV curves with characteristic H3-shaped hysteresis loops of mesoporous structures according to the IUPAC classification. The BET specific surface areas of Bi_2NbO_5F and Bi_2TaO_5F samples are 33.1 and 21.0 $m^2 \cdot g^{-1}$, respectively. The inset panels display the pore size distribution curves derived from the desorption branch using BJH model. A sharp peak located at $30 \sim 40$ nm can be observed, which is derived from the interlaced nanoplates. Additionally, there exists another broad peak at about $200 \sim 300$ nm, which may be resulted from the packing of those spheres. The BJH desorption average pore diameter is calculated to be 21.7 and 24.2 nm for Bi_2NbO_5F and Bi_2TaO_5F, respectively.

3.5. Optical absorption property

UV–vis diffuse reflectance spectroscopy has also been applied to investigate the optical absorption and determine the optical band gap of the prepared Bi_2NbO_5F and Bi_2TaO_5F samples. As shown in Fig. 6, in both spectra, a steep absorption edge can be clearly detected, which always implies the intrinsic interband transition [34]. However, following the intense absorption edge in the near-
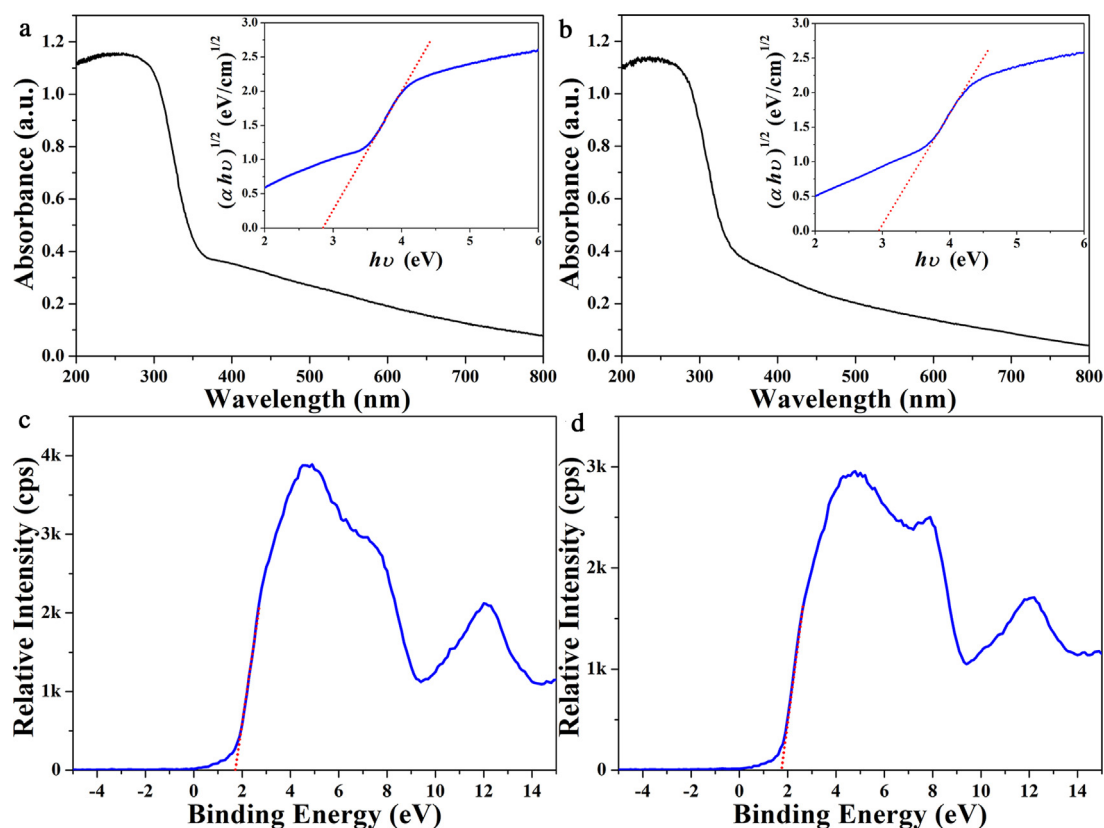
Fig. 6. UV–vis diffuse reflectance spectra of the as-synthesized (a) Bi_2NbO_5F and (b) Bi_2TaO_5F hierarchical hollow spheres. The insets are the corresponding plot of $(\alpha h\upsilon)^{1/2}$ *vs.* photon energy ($h\upsilon$). VB-XPS spectra of the as-prepared (c) Bi_2NbO_5F and (d) Bi_2TaO_5F hierarchical hollow spheres.

UV region, a weak visible light absorption even can be detected, which is definitely not due to the band-gap transition, but probably due to the transition from the impurity level arising from lattice defects and the distortion of crystal faces. For a crystalline semiconductor, the optical absorption near the band edge follows the equation $\alpha h\upsilon = A(h\upsilon - E_g)^{n/2}$, where α, $h\upsilon$, A and E_g are the absorption coefficient, the photonic energy, a proportionality constant, and the band gap energy, respectively, and the value of n is associated with the transition type of the semiconductor ($n = 1$ and 4 for direct and indirect transition, respectively). To measure the optical band gap (E_g) of the fabricated Bi_2NbO_5F and Bi_2TaO_5F materials, the plots of $(\alpha h\upsilon)^{1/2}$ versus ($h\upsilon$) are displayed in the insets of Fig. 6a and b, respectively. In the absorption edge region, the plots are nearly linear, suggesting that the absorption edge of both materials should be attributed to the indirect transition. By extrapolating the straight line to zero absorption, the band gaps of the prepared Bi_2NbO_5F and Bi_2TaO_5F hierarchical hollow spheres are estimated to be 2.86 and 2.95 eV, respectively. This is the first time that the experimental band gap values of Bi_2NbO_5F or Bi_2TaO_5F materials are reported. To better elucidate the band structures of the prepared Bi_2NbO_5F and Bi_2TaO_5F materials, VB-XPS was measured to determine the position of the Fermi level with respect to the valence band maximum (VBM). The VB-XPS spectra near the Fermi level for Bi_2NbO_5F and Bi_2TaO_5F samples are illustrated in Fig. 6c and d, respectively. The main peak centered at the low binding energy of ~4.7 eV can be attributed to O 2p derived VB states. Generally, by extrapolating the leading edge of the O 2p derived VB to its intersection with background counts near the Fermi level, the VBM value can be estimated. Accordingly, the VBM potentials of 1.72 eV and 1.76 eV can be obtained for the as-prepared Bi_2NbO_5F and Bi_2TaO_5F samples, respectively. Combined with the band gaps discussed above, the conduction band minimum (CBM) of the pre-
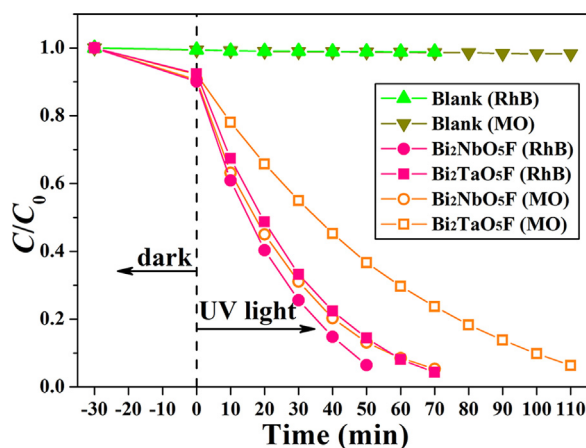

Fig. 7. Photodegradation of RhB and MO under UV-light irradiation as a function of the irradiation time without catalyst (blank), and over the as-prepared Bi_2MO_5F (M = Nb, Ta) hierarchical hollow spheres.

pared Bi_2NbO_5F and Bi_2TaO_5F samples would occur at -1.14 eV and -1.19 eV, respectively.

3.6. UV-light photocatalytic activity

The photocatalytic performance of the obtained Bi_2NbO_5F and Bi_2TaO_5F hierarchical hollow spheres was evaluated by photodegradation of RhB and MO under both UV- and visible-light irradiation. For the UV-light photodegradation of RhB and MO, the variations of dye concentration (C/C_0) with irradiation time are plotted in Fig. 7, where C_0 and C are the initial and instant concentrations of dye, respectively. In dark adsorption-desorption
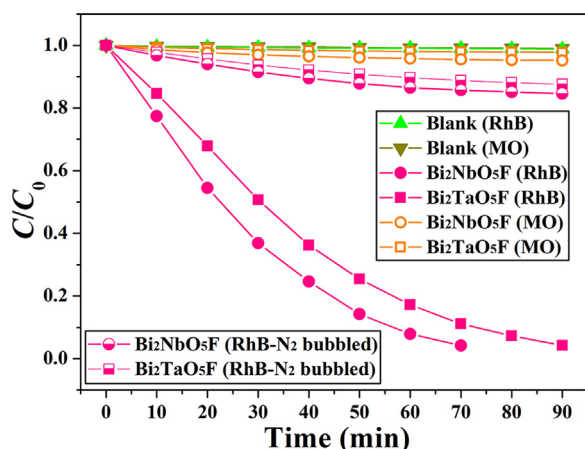
Fig. 8. Photodegradation of RhB and MO under visible-light irradiation as a function of the irradiation time without catalyst (blank), and over the as-prepared Bi_2MO_5F (M = Nb, Ta) hierarchical hollow spheres.

Fig. 9. Wavelength-dependent activities for photodegradation of RhB under visible-light irradiation over the as-prepared Bi_2MO_5F (M = Nb, Ta) hierarchical hollow spheres.

equilibration, Bi_2NbO_5F shows slightly higher dye adsorption than Bi_2TaO_5F, thanks to the larger surface area. Under UV-light irradiation, the degradation of RhB and MO is almost negligible in the absence of catalyst (blank). With introduction of the photocatalysts (Bi_2NbO_5F or Bi_2TaO_5F), an efficient degradation of dyes can be observed owing to the photoexcitation of photocatalysts to form electrons and holes, which can react with O_2, H_2O or OH^- to generate $\cdot OH$ radicals to degrade dyes. The photodegradation efficiencies of RhB are 94% within 50 min of irradiation on Bi_2NbO_5F and 96% within 70 min of irradiation on Bi_2TaO_5F. While for MO, the efficiencies are 95% within 70 min of irradiation on Bi_2NbO_5F and 94% within 110 min of irradiation on Bi_2TaO_5F. For the same dye, Bi_2NbO_5F exhibits better photodegradation efficiency than Bi_2TaO_5F does. For the same photocatalyst, RhB can be degraded more easily than MO. The photoreaction rate constants can be calculated by the pseudo-first-order kinetic model: $\ln(C_0/C) = kt$, where the rate constant k is determined from the slope of the linear relationship of $\ln(C_0/C)$ *vs* t (Fig. S9). Apparently, the rate constant for RhB photodegradation by Bi_2NbO_5F is the highest ($0.050 \, min^{-1}$). In our precious work, RhB was degraded within 75 min under UV-light irradiation, using hierarchical BiF_3–Bi_2NbO_5F composite as the catalyst, which have a bandgap of 3.47 eV [33]. Single-phase Bi_2NbO_5F exhibits better photocatalytic activity than BiF_3–Bi_2NbO_5F composites, since BiF_3 has a large band gap (3.81 eV) [35].

3.7. Visible-light photocatalytic activity

The photodegradation of RhB and MO by as-prepared Bi_2NbO_5F and Bi_2TaO_5F samples were also studied under visible-light irradiation (Fig. 8). It is interesting to note that the photodegradation efficiency can reach 96% for RhB, but is less than 5% for MO. Similarly, Bi_2NbO_5F has a faster photoreaction rate constant than Bi_2TaO_5F in visible-light degradation of RhB (Fig. S10). It is well-known that some special dyes, such as RhB and phthalocyanine derivates, can be degraded under visible-light by self-photosensitization over semiconductors with a wide band gap. Usually, MO can hardly be self-photosensitized and is always photodegraded from the photocatalytic reaction. Previously, we have demonstrated the visible-light photosensitized degradation of RhB mediated by the hierarchical BiF_3–Bi_2NbO_5F composite [33]. Therefore, it is rational to believe that the visible light degradation of RhB by the prepared Bi_2NbO_5F and Bi_2TaO_5F in this research is also an indirect dye photosensitization process. As we know, O_2 is indispensable in the photosensitization degradation reaction
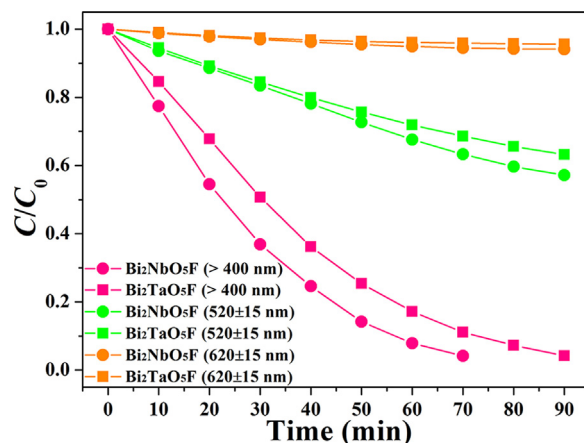
[36]. To confirm the photosensitization process, the visible-light photodegradation of RhB under N_2-bubbled condition was also performed for comparison. To be specific, before illumination, the suspension was bubbled with N_2 for 1 h to exhaust the dissolved O_2 and the N_2-purging process was continued until the ceasing of degradation reaction. The results reveal that a dramatic drop in degradation efficiency of RhB occurs when O_2 is excluded by N_2-purging. Consequently, it is believed that the electron transfer via O_2 plays a critical role in this photodegradation reaction. Herein, RhB acts as a photosensitizer, and Bi_2MO_5F then plays the roles of electron carrier and acceptor. In detail, it has been known that RhB (+0.95 V *vs* NHE) can be excited to RhB* (−1.42 V *vs* NHE) [37] when irradiated by visible light. Apparently, the potential of RhB* is more negative than the potential of CB electrons of Bi_2NbO_5F (−1.14 V) and Bi_2TaO_5F (−1.19 V). Consequently, the electrons from the excited states of RhB* can be spontaneously injected into the conduction band of Bi_2MO_5F with the conversion of RhB to the cationic radicals ($\cdot RhB^+$). After then, these injected electrons can react with the surface-adsorbed O_2 molecules to yield $\cdot O_2^-$ radical anion species and subsequently $\cdot OH$ and $\cdot OOH$ radicals by protonation, which ultimately react with $\cdot RhB^+$ to induce the degradation of RhB.

As we know, the dye self-sensitized process occurs on visible-light photoexcitation. To provide further evidence on the indirect dye photosensitization process in the visible-light photodegradation of RhB, the wavelength-dependent experiments were investigated by tuning the excitation wavelength with band pass filters of 520 ± 15 nm (DT520) and 620 ± 15 nm (DT620) (Beijing NBeT Technology Co., Ltd.). It is known that the required energy (wavelength) to excite RhB molecules is ~554 nm. Therefore, when the 520 ± 15 nm filter is used, only RhB molecules can be excited, while both Bi_2NbO_5F and Bi_2TaO_5F catalysts would have no response in this condition based on their band gaps. As shown in Fig. 9, the photodegradation efficiencies of RhB still reach 43% and 37% by the prepared Bi_2NbO_5F and Bi_2TaO_5F samples, respectively. However, as the filter is changed to be 620 ± 15 nm, the total dye degradation is negligible, because both RhB and catalysts cannot respond to this light. These results further demonstrate that the visible-light photodegradation of RhB by Bi_2NbO_5F and Bi_2TaO_5F samples should be attributed to the photosensitization mechanism.

3.8. TOC and stability analyses

Generally, decolorization does not mean the complete oxidization of dyes into harmless final products such as CO_2 and H_2O.
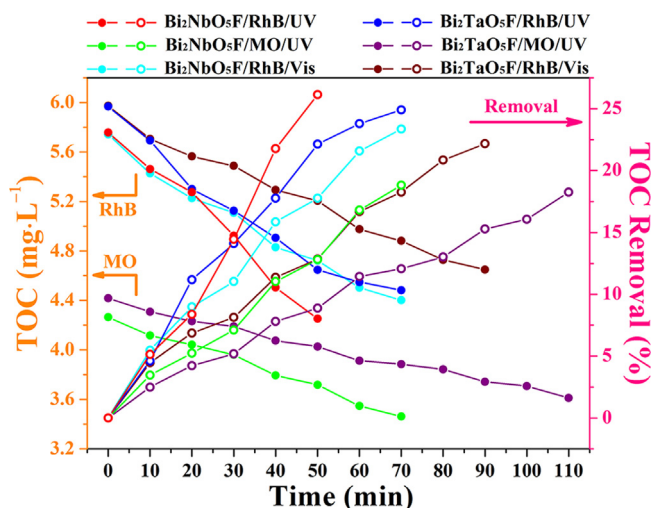
Fig. 10. TOC and TOC removal as a function of light irradiation time during the photodegradation of RhB and MO by the prepared Bi_2MO_5F (M = Nb, Ta) catalysts under both UV- and visible-light irradiation.

Therefore, TOC removals of dyes are usually employed to determine the degree of mineralization during photolysis. Fig. 10 gives the TOC concentration and TOC removal of RhB and MO during the UV- and visible-light irradiation periods after adsorption–desorption equilibrium. It can be found that the TOC removal process is greatly slower than the decolorization one. Although all the treated dye solutions are almost colorless, the TOC removal efficiencies are just about 22–26% for RhB solutions and 18 ∼ 19% for MO solutions. It has been reported that the complete mineralization of dyes usually goes through two different stages: the initial cleavage of the chromophoric groups of the dyes, and the subsequent oxidation of the fragments in the latter stage which requires for a longer time [38,39]. The TOC results suggest that the photomineralization of RhB and MO dyes by the prepared Bi_2NbO_5F and Bi_2TaO_5F catalysts is possible.

As a kind of heterogeneous photocatalysts, the recycling stability of them is particularly important for their application. In order to study the photostability of the prepared Bi_2NbO_5F and Bi_2TaO_5F catalysts, the recycling experiments for the photodegradation of RhB and MO under UV- and visible-light irradiation were also performed. After each run of photoreaction, the catalyst was centrifuged out, washed with distilled water and then re-dispersed into 100 mL of the new dye aqueous solution with the initial concentration ($10\,mg\,L^{-1}$). As displayed in Fig. S11, after five cycling runs of photoreactions, only about 2 ∼ 3% decrease in photodegradation ratio can be found, which reveals that the obtained Bi_2NbO_5F and Bi_2TaO_5F hierarchical hollow spheres are stable during the photodegradation of dyes.

4. Conclusions

In conclusion, a low-temperature solution method has been developed in fabrication of Aurivillius-type layered oxyfluoride perovskites Bi_2NbO_5F and Bi_2TaO_5F. The products were composed of hierarchical hollow spheres with relatively high surface area. The formation and growth mechanism were investigated through the time-dependent phase and morphology evolution processes. The UV–vis diffuse reflectance spectra showed that the prepared Bi_2NbO_5F and Bi_2TaO_5F samples have the indirect band gaps of 2.86 and 2.95 eV, respectively. The photodegradation tests demonstrated that the obtained Bi_2NbO_5F and Bi_2TaO_5F hierarchical hollow spheres could be effectively served as catalysts for the degradation of RhB and MO under UV-light irradiation via the

photocatalytic reaction. Additionally, they also could be applied in visible-light degradation of RhB via the photosensitization process. The facile synthetic approach adopted in this work can be expected to be extendable to the general synthesis of various oxyfluoride perovskites.

Acknowledgments

Appendix A. Supplementary data

Supplementary data associated with this article can be found, in the online version, at http://dx.doi.org/10.1016/j.apcatb.2016.12.029.

References

[1] Y. Tsujimoto, K. Yamaura, E. Takayama-Muromachi, Oxyfluoride chemistry of layered perovskite compounds, Appl. Sci. 2 (2012) 206–219.
[2] B. Aurivillius, Mixed bismuth oxides with layer lattices. 2. Structure of $Bi_4Ti_3O_{12}$, Ark. Kemi 1 (1949) 499–512.
[3] J. Hauck, K. Mika, G. Krabbes, Search for new high-T_c oxide structures, Phys. C 185–189 (1991) 721–722.
[4] W. Zhou, P.A. Andersen, C. Lin, P. Edwards, Two perovskite-related materials for future superconductivity, Phys. C 190 (1991) 59–61.
[5] N.I. Medvedeva, S.A. Turzhevsky, V.A. Gubanov, A.J. Freeman, Electronic structure of Aurivillius phases: ideal Bi_2NbO_6, its stabilization with fluorine substitution and the role of oxygen vacancies, Phys. Rev. B 48 (1993) 16061–16067.
[6] N.I. Medvedeva, V.A. Gubanov, Electronic structure and properties of Aurivillius phases, J. Struct. Chem. 37 (1996) 409–416.
[7] B. Aurivillius, The structure of Bi_2NbO_5F and isomorphous compounds, Ark. Kemi 5 (1952) 39–47.
[8] R.L. Needs, S.E. Dann, M.T. Weller, J.C. Cherryman, R.K. Harris, The structure and oxide/fluoride ordering of the ferroelectrics $Bi_2TiO_4F_2$ and Bi_2NbO_5F, J. Mater. Chem. 15 (2005) 2399–2407.
[9] E.E. McCabe, I.P. Jones, D. Zhang, N.C. Hyatt, C. Greaves, Crystal structure and electrical characterisation of Bi_2NbO_5F: An Aurivillius oxide fluoride, J. Mater. Chem. 17 (2007) 1193–1200.
[10] F.A. Mirishli, I.H. Ismailzade, Synthesis and study of new lamellar ferroelectrics, Izv. Akad. Nauk. SSSR Ser. Fiz. 35 (1971) 1833–1837.
[11] I.H. Ismailzade, J. Ravez, $Bi_2TiO_4F_2$–A new one-layer perovskite-like ferroelectric, Ferroelectrics 21 (1978) 423–424.
[12] B. Erdinc, E. McCabe, D. Duran, M.N. Secuk, S.E. Gulebaglan, E.K. Dogan, M. Aycibin, H. Akkus, Calculation of electronic band structure of ferroelectric semiconductor bismuth niobium oxyfluoride (Bi_2NbO_5F) crystal, GU J. Sci. 27 (2014) 1099–1103.
[13] D. Duran, B. Erdinc, M. Aycibin, H. Akkus, Linear optical properties of ferroelectric semiconductor Bi_2NbO_5F crystal, Ferroelectrics 486 (2015) 25–32.
[14] H. Kodama, F. Izumi, A. Watanabe, New members of a family of layered bismuth compounds, J. Solid State Chem. 36 (1981) 349–355.
[15] S.Y. Wang, B.B. Huang, Z.Y. Wang, Y.Y. Liu, W. Wei, X.Y. Qin, X.Y. Zhang, Y. Dai, A new photocatalyst: $bi_2TiO_4F_2$ nanoflakes synthesized by a hydrothermal method, Dalton Trans. 40 (2011) 12670–12675.
[16] B. Jiang, P. Zhang, Y. Zhang, L. Wu, H.X. Li, D.Q. Zhang, G.S. Li, Self-assembled 3D architectures of $Bi_2TiO_4F_2$ as a new durable visible-light photocatalyst, Nanoscale 4 (2012) 455–460.
[17] D. Ravelli, D. Dondi, M. Fagnoni, A. Albini, Photocatalysis. A multi-faceted concept for green chemistry, Chem. Soc. Rev. 38 (2009) 1999–2011.
[18] C.C. Chen, W.H. Ma, J.C. Zhao, Semiconductor-mediated photodegradation of pollutants under visible-light irradiation, Chem. Soc. Rev. 39 (2010) 4206–4219.
[19] H. Tong, S.X. Ouyang, Y.P. Bi, N. Umezawa, M. Oshikiri, J.H. Ye, Nano-photocatalytic materials: possibilities and challenges, Adv. Mater. 24 (2012) 229–251.
[20] A. Kubacka, M. Fernández-García, G. Colón, Advanced nanoarchitectures for solar photocatalytic applications, Chem. Rev. 112 (2012) 1555–1614.
[21] X.B. Chen, S.H. Shen, L.J. Guo, S.S. Mao, Semiconductor-based photocatalytic hydrogen generation, Chem. Rev. 110 (2010) 6503–6570.

[22] T. Hisatomi, J. Kubota, K. Domen, Recent advances in semiconductors for photocatalytic and photoelectrochemical water splitting, Chem. Soc. Rev. 43 (2014) 7520–7535.

[23] C.E. Mohn, S. Stølen, Influence of the stereochemically active bismuth lone pair structure on ferroelectricity and photocalytic activity of Aurivillius phase Bi_2WO_6, Phys. Rev. B 83 (2011) 014103.

[24] S.M. Sun, W.Z. Wang, Advanced chemical compositions and nanoarchitectures of bismuth based complex oxides for solar photocatalytic application, RSC Adv. 4 (2014) 47136–47152.

[25] W. Wang, M.O. Tadé, Z.P. Shao, Research progress of perovskite materials in photocatalysis- and photovoltaics-related energy conversion and environmental treatment, Chem. Soc. Rev. 44 (2015) 5371–5408.

[26] N. Zhang, R. Ciriminna, M. Pagliaro, Y.J. Xu, Nanochemistry-derived Bi_2WO_6 nanostructures: towards production of sustainable chemicals and fuels induced by visible light, Chem. Soc. Rev. 43 (2014) 5276–5287.

[27] Y.X. Li, G. Chen, H.J. Zhang, Z.S. Lv, Band structure and photocatalytic activities for H_2 production of $ABi_2Nb_2O_9$ (A = Ca, Sr Ba), Int. J. Hydrogen Energy 35 (2010) 2652–2656.

[28] D.F. Hou, W. Luo, Y.H. Huang, J.C. Yu, X.L. Hu, Synthesis of porous $Bi_4Ti_3O_{12}$ nanofibers by electrospinning and their enhanced visible-light-driven photocatalytic properties, Nanoscale 5 (2013) 2028–2035.

[29] S.M. Sun, W.Z. Wang, H.L. Xu, L. Zhou, M. Shang, L. Zhang, $Bi_5FeTi_3O_{15}$ hierarchical microflowers: hydrothermal synthesis, growth mechanism, and associated visible-light-driven photocatalysis, J. Phys. Chem. C 112 (2008) 17835–17843.

[30] G. Naresh, T.K. Mandal, Excellent sun-light-driven photocatalytic activity by Aurivillius layered perovskites $Bi_{5−x}La_xTi_3FeO_{15}$ (x = 1, 2), ACS Appl. Mater. Interfaces 6 (2014) 21000–21010.

[31] X.N. Li, Z. Ju, F. Li, Y. Huang, Y.M. Xie, Z.P. Fu, R.J. Knize, Y.L. Lu, Visible light responsive $Bi_7Fe_3Ti_3O_{21}$ nanoshelf photocatalysts with ferroelectricity and ferromagnetism, J. Mater. Chem. A 2 (2014) 13366–13372.

[32] C.D. Wagner, W.M. Riggs, L.E. Davis, J.F. Moulder, G.E. Muilenberg, Handbook of X-ray Photoelectron Spectroscopy, 1st ed., Perkin-Elmer, Minnesota, 1979.

[33] S.J. Lei, C.N. Wang, D. Cheng, X.J. Gao, L.F. Chen, Y.T. Yan, J.L. Zhou, Y.H. Xiao, B.C. Cheng, Hierarchical $BiF_3−Bi_2NbO_5F$ core–shell structure and its application in the photosensitized degradation of rhodamine b under visible light irradiation, J. Phys. Chem. C 119 (2015) 502–511.

[34] M. Jansen, H.P. Letschert, Inorganic yellow-red pigments without toxic metals, Nature 404 (2000) 980–982.

[35] C. Ortiz, O. Eriksson, M. Klintenberg, Data mining and accelerated electronic structure theory as a tool in the search for new functional materials, Comput. Mater. Sci. 44 (2009) 1042–1049.

[36] T.X. Wu, G.M. Liu, J.C. Zhao, Photoassisted degradation of dye pollutants. V. Self-photosensitized oxidative transformation of Rhodamine B under visible light irradiation in aqueous TiO_2 dispersions, J. Phys. Chem. B 102 (1998) 5845–5851.

[37] T. Shen, Z.G. Zhao, Q. Yu, H.J. Xu, Photosensitized reduction of benzil by heteroatom-containing anthracene dyes, J. Photochem. Photobiol. A: Chem. 47 (1989) 203–212.

[38] H.B. Fu, C.S. Pan, W.Q. Yao, Y.F. Zhu, Visible-light-induced degradation of rhodamine B by nanosized Bi_2WO_6, J. Phys. Chem. B 109 (2005) 22432–22439.

[39] N.F. Jaafar, A.A. Jalil, S. Triwahyono, M.N.M. Muhid, N. Sapawe, M.A.H. Satar, H. Asaari, Photodecolorization of methyl orange over (-Fe_2O_3-supported HY catalysts: the effects of catalyst preparation and dealumination, Chem. Eng. J. 191 (2012) 112–122.